Original Article

The Protective Function of Directed Asymmetry in the Pericellular Matrix Enveloping Chondrocytes

SCOTT C. SIBOLE [iD],[1] ENG KUAN MOO,[1,2] SALVATORE FEDERICO,[1,3]
and WALTER HERZOG[1,3]

[1]Human Performance Laboratory, University of Calgary, Calgary, Canada; [2]Department of Applied Physics, University of Eastern Finland, Kuopio, Finland; and [3]Department of Mechanical and Manufacturing Engineering, University of Calgary, Calgary, Canada

Associate Editor Stefan M. Duma oversaw the review of this article.

Abstract—The specialized pericellular matrix (PCM) surrounding chondrocytes within articular cartilage is critical to the tissue's health and longevity. Growing evidence suggests that PCM alterations are ubiquitous across all trajectories of osteoarthritis, a crippling and prevalent joint disease. The PCM geometry is of particular interest as it influences the cellular mechanical environment. Observations of asymmetrical PCM thickness have been reported, but a quantified characterization is lacking. To this end, a novel microscopy protocol was developed and applied to acquire images of the PCM surrounding live cells. Morphometric analysis indicated a statistical bias towards thicker PCM on the inferior cellular surface. The mechanical effects of this bias were investigated with multiscale modelling, which revealed potentially damaging, high tensile strains in the direction perpendicular to the membrane and localized on the inferior surface. These strains varied substantially between PCM asymmetry cases. Simulations with a thicker inferior PCM, representative of the observed geometry, resulted in strain magnitudes approximately half of those calculated for a symmetric geometry, and a third of those with a thin inferior PCM. This strain attenuation suggests that synthesis of a thicker inferior PCM may be a protective adaptation. PCM asymmetry may thus be important in cartilage development, pathology, and engineering.

Keywords—Articular cartilage, Laser scanning microscopy, Pericellular matrix, Chondrocyte, Multiscale model.

Address correspondence to Scott C. Sibole, Human Performance Laboratory, University of Calgary, Calgary, Canada. Electronic mail: ssibole@ucalgary.ca

Scott C. Sibole and Eng Kuan Moo have contributed equally to this work.

INTRODUCTION

Articular cartilage (AC) is an elegant natural solution to meet the harsh mechanical demands placed on the diarthrodial joints of the musculoskeletal system. Through an intricate solid-fluid material composition and architecture it provides nearly frictionless lubrication, improved load distribution, and exceptional wear resistance.[11] Unfortunately, articular cartilage is also one of the first tissues to undergo degeneration in debilitating joint diseases such as osteoarthritis. Cartilage degeneration has been thought to be a result of biochemical and/or biomechanical insult, but its initiation and trajectory can vary, leading to the definition of several disease subtypes.[15,17] However, alterations to the thin (2–4 μm) pericellular matrix (PCM), a specialized tissue region surrounding chondrocytes (cartilage cells),[12] have been proposed as a unifying pathological feature.[21] Observations from transgenic[2,64] and injury-induced[42] osteoarthritic animal models offer strong support to this hypothesis. Of particular interest, recent experimental observations found that PCM mechanics were altered before all other major tissue components in the very early stages of post-traumatic osteoarthritis (as early as 3 days post injury).[7] As such, the development of therapeutic interventions to maintain a healthy PCM may be an ideal target to halt or slow cartilage degeneration near its initiation.

Whereas the extracellular matrix (ECM) that comprises the majority of the cartilage volume is composed mainly of collagen type II and the chondroiton-sulfate proteoglycan, aggrecan,[11] the PCM consists of type VI

collagen and interspersed heparan-sulfate and leucine-rich proteoglycans (such as biglycan, decorin, and perlecan).[63] The distinct structure and composition of the PCM serve to regulate the mechanical and chemical microenvironment of the chondrocytes. Collectively, the PCM and all cells it encapsulates are referred to as a chondron. Mechanically, the PCM attenuates high magnitude strains in the soft superficial zone tissue and amplifies small magnitude strains in the stiff tissue of the middle and deep zones[9] such that the cells experience deformation large enough for proper mechanoregulation, but not so large as to exceed their viable limits. Additionally, the unique proteoglycan content of the PCM influences the osmotic environment of the cell,[64] which is known to be a strong regulator of chondrocyte physiology.[19,41] Biochemically, the heparan-sulfate side chains of the proteoglycans help regulate growth factor secretion[5,10,49] and the integrin protein machinery that allow for cellular attachment to the surrounding collagen matrix.[28,52,54]

Despite extensive studies on the biophysics and biochemistry of the PCM, various aspects remain unexplored. For example, microscopic studies of PCM showed that the radial thickness is uneven around the perimeter of chondrocytes residing in native cartilage.[44,62] Such observations may appear insignificant at first sight, but gain intrigue with consideration that newly formed PCM in tissue-engineered constructs have highly uniform and symmetric thickness (Fig. 1).[13]

Notably, the cells that produced this symmetric PCM were not subjected to mechanical loading. The hypothesis thus follows that the formation of an asymmetric PCM may be directed by the cell in response to mechanical stimuli translated from joint loading; however, this has not been explored. As an initial step, two major questions should be addressed with regard to PCM asymmetry. Firstly, is the asymmetry directionally dependent? Since the mechanics of articular cartilage are both of the highest magnitude and of the greatest variability in the superficial zone near the cartilage surface, adaptation in PCM geometry in response to mechanics should be most pronounced with respect to tissue depth. Secondly, if the asymmetry is directed, what mechanical changes does it instill? These mechanical effects of asymmetry, should they exist, are expected to directly impact the cell as it is the mediator of PCM formation. To explore these questions, two study objectives were proposed: (1) to develop and apply an imaging and segmentation methodology for the identification and morphological quantification of the PCM in articular cartilage containing living cells, and (2) to explore the mechanical effects of the quantified morphology through the development and application of a modelling and simulation protocol.

METHODS

Specimen Preparation

Fresh osteochondral blocks (5 mm × 5 mm) were excised from the load-bearing surfaces of medial femoral grooves harvested from skeletally mature New Zealand white rabbits (10-12 month-old, $N_{animal} = 6$) approved for research use by the university ethics review board. The extracellular matrix (ECM) and live cells of the AC were fluorescently stained using 16 μM 5-(4,6-dichlorotriazinyl) aminofluorescein (5-DTAF, Ex:492 nm, Em:516 nm, Thermo Fisher Scientific Inc,
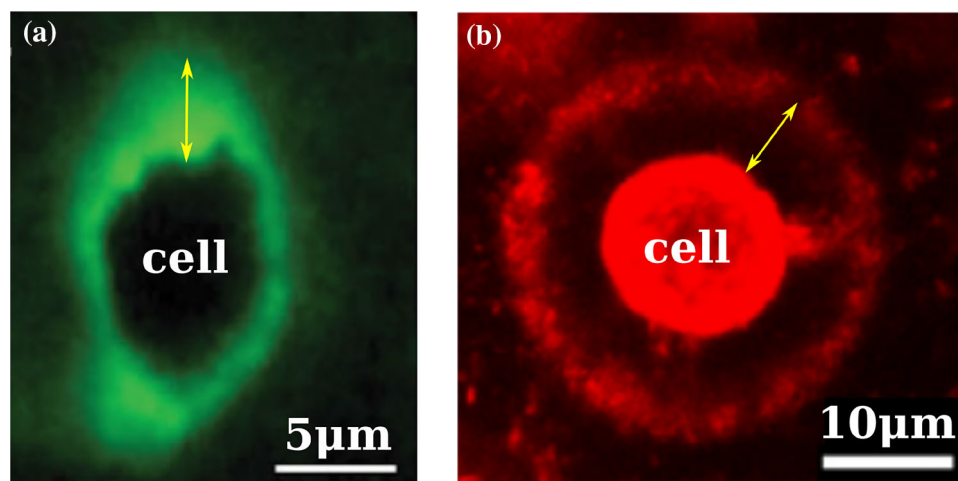
FIGURE 1. Morphologies of *in situ* (a) and newly-grown (b) PCM, as indicated by the yellow double arrow, are distinctly different. PCM was located by immunostaining of type VI collagen in both cases. *In situ* PCM has non-uniform thickness around a cell, but newly-grown PCM surrounds a cell with a uniform distribution (adapted from Refs. 62 and 13 with permission).
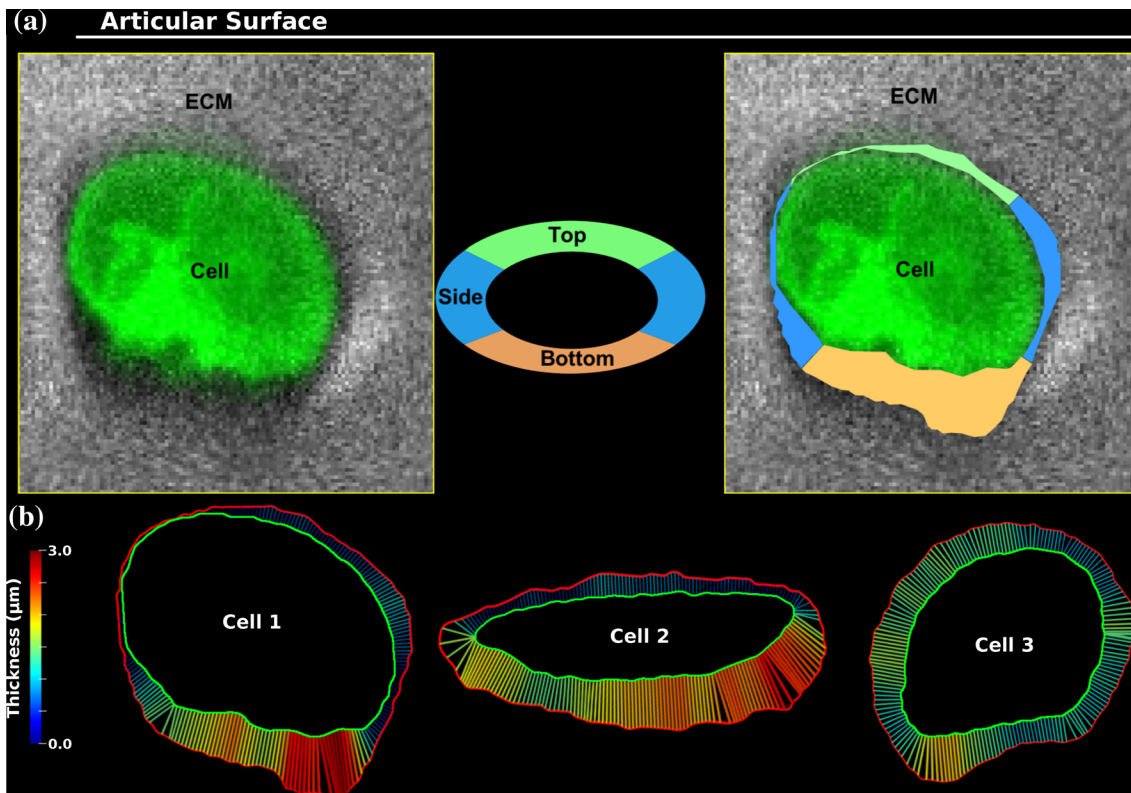
FIGURE 2. (a—Left) Raw image showing a live cell (green) separated from the ECM (grey) by a layer of PCM (black); (a—Middle) division of PCM layer into 'top', 'side' and 'bottom' layers based on cell orientation relative to the articular surface; (a—Right) Segmented image showing the top, side, and bottom layers of PCM, (b) PCM thickness of three selected chondrons indicating that the 'top' PCM layer was thinner than the 'bottom' layer. The chondrons and cells are outlined in red and blue colours, respectively. Only cells in the superficial zone were considered in this study.

MA, USA) and 3 μM Calcein Red/Orange AM (Ex:577 nm, Em:590 nm, Thermo Fisher Scientific Inc, MA, USA), respectively, in a phosphate buffered saline solution for 1h. Following the staining, the specimens were washed three times in a dye-free saline solution to remove excess dye. The blocks were then attached to a specimen holder using dental cement with careful alignment of the articular surface to the horizontal plane. Specimens were kept hydrated in a dye-free saline for the subsequent imaging protocol.

Multi-photon imaging protocol

The ECM and live cells with the cartilage specimens were simultaneously imaged using a two-photon excitation (TPE) imaging technique. TPE imaging was chosen as it minimizes photobleaching artifacts and allows for greater light penetration depth.[34,65] The osteochondral specimens were scanned under an upright multi-photon laser scanning microscope (FVMPE-RS model, Olympus, Tokyo, Japan) equipped with a wavelength-tunable (680-1300 nm), ultra-short-pulsed (pulse width: <120fs; repetition rate: 80 MHz) laser (InSight DeepSee-Ol, Spectra-Physics, CA,

USA) and a 25x/1.05 NA glass-corrected water immersion objective (XLPLN25XWMP2 model, Olympus, Tokyo, Japan). The excitation laser wavelength was set at 800 nm. The resulting TPE signals emitted by the ECM and live cells were simultaneously collected in the backward (epi-) direction and separated by a dichroic beam splitter (FF570-Di01, Semrock Inc., USA), before being band-pass filtered at wavelengths of 516 nm (FF01 518/45, Semrock Inc., NY, USA) and 590 nm (FF01 610/70, Semrock Inc., NY, USA), respectively. A series of planar images were acquired in the horizontal plane (xy-plane; imaging area: 127×127 μm^2, pixel size:0.16 μm; bit-depth: 12; dwell time: 2 μs) along the objective axis at 1 μm intervals. Image stacks spanned from the surface of the articular cartilage to a depth of 50 μm. The PCM layer can be visualized as the unstained dark region in images constructed by the merging of the acquired ECM and cellular signals (Fig. 2a).

Image Processing, Segmentation, and Analysis

Only chondrons containing a single cell were selected for characterization. The mid-section of the

image stack containing a chondron was used for planar image analysis. Custom Python software utilizing Simple Insight Toolkit[31] and Visualization Toolkit[48] were developed to complete the image processing, segmentation, and analysis tasks. Segmentation of both the cell and the ECM from selected chondron regions within images from each channel, respectively, was performed using Otsu's thresholding method.[43] However, prior to this segmentation, ECM and cellular channels were processed differently. A bilateral filter[55] was applied to the regions of interest in the ECM images, followed by adaptive contrast equalization,[51] intensity inversion, and small exponentiation of the pixel intensities to enhance contrast. The inversion of the image resulted in the chondron being in the foreground. For the cellular channel, smoothing with curvature-based anisotropic diffusion[60] was sufficient. Images were converted to 32-bit floating point precision prior to all processing steps. Isocontours were extracted from the processed ECM and cellular channels at the determined threshold values using marching squares. These represented the boundary of the chondron and cells, respectively.

The determination of PCM thicknesses from the chondron and cellular isocontours was achieved with a two-step process. Firstly, the directions of thickness measurements were defined as the surface normals on the convex hull of the chondron. Ray-casting was then used to determine the intersection points with the chondron and cell contours along these directions. The thicknesses were defined as the distance between each of these intersection point pairs. Using this technique, measurement artifacts due to rapid curvature changes, concavities in the contours, or large differences in local cell and chondron contour shapes were avoided. A total of 355 chondrons from 6 animals were used. The quantified PCM thickness measurements were then stratified as either 'top', 'side', or 'bottom' with respect to the AC surface ('top') (Fig. 2a). This grouping was based on the angular direction, θ, of thickness measurement vectors relative to the cartilage surface ($\theta = 0$) with bins defined in Table 1.

TABLE 1. The grouping of thickness measurements were defined by their angular direction, θ, relative to the cartilage surface orientation ($\theta = 0$).

Region	Domain
Top	$\frac{\pi}{4} < \theta \leq \frac{3\pi}{4}$
Bottom	$\frac{5\pi}{4} < \theta \leq \frac{7\pi}{4}$
Side	$\frac{-\pi}{4} < \theta \leq \frac{\pi}{4}$
	$\frac{3\pi}{4} < \theta \leq \frac{5\pi}{4}$

Statistical Analysis

Statistical analyses were performed using SPSS (version 25, SPSS Inc. IL, USA). The results were expressed as estimated marginal means (EMM) $\pm$ 1 standard error. The mean value of PCM thickness was analyzed for the effect of relative PCM location with respect to cell (i.e., either top, side or bottom location relative to the cell) using a generalized estimating equation (GEE, under Genlin Mixed procedures in SPSS) to take into account the correlated (measurements within individual animals) nature of the observations and the unbalanced (unequal number of analyzed cells for each animal) design of the study. All statistical tests were performed for two-sided testing with a type I error acceptance level, $\alpha = 0.05$. Multiple comparisons were accounted for through sequential Bonferroni adjusted *p*-values. As long as the data were interval-type, no assumptions regarding normal distribution were necessary for the GEE statistical method.

Modelling and Simulation

A multiscale modelling procedure was employed to investigate the effects of PCM asymmetry. This consisted of firstly, the definition and solution of a tissue scale model. Multiple cellular scale models were then generated with different geometries. The boundary conditions of the cellular scale models were derived from the solution of the tissue scale model through linear interpolation, thus providing a coupling between the tissue and cellular scales. This technique allowed for investigation of cellular scale mechanics at multiple locations in the tissue volume by simply rigidly translating the cellular scale geometries to different positions in the domain of the tissue scale model and repeating the boundary condition interpolation. A Python module was developed to automate this procedure.

The physics of the model at both scales were governed by the quasi-static balance of linear momentum assuming zero body forces,

$$div\, \boldsymbol{\sigma} = \mathbf{0}, \tag{1}$$

where $\boldsymbol{\sigma}$ is the Cauchy stress field. In articular cartilage, both solid and fluid phases contribute to this stress field, as described by the popular biphasic mixture theory,

$$\boldsymbol{\sigma} = \boldsymbol{\sigma}_e - p\mathbf{i}, \tag{2}$$

where $\boldsymbol{\sigma}_e$ is effective or solid phase stress, p is the fluid pressure, and $\mathbf{i}$ is the identity.[25,39,56] Enforcing conservation of mass and linear momentum on the mixture and fluid, respectively, leads to Darcy's Law,

$$\mathbf{w} = -\mathbf{k}\,grad\,p, \tag{3}$$

where $\mathbf{w}$ is the fluid flux and $\mathbf{k}$ is the second-order hydraulic permeability tensor, which may depend on deformation. With the additional specification of constitutive laws and boundary conditions, these equations can be solved. All model solutions in this study were obtained with the finite element method as implemented in the open source software package, *FEBio*.[32]

Constitutive Laws

All solid phase constitutive laws in this study adopt a hyperelastic formulation. Here the stress-strain relationship is defined as the derivative of a scalar-valued strain energy function, $\psi(\mathbf{F}(\mathbf{X}), \mathbf{X})$, with respect to the deformation gradient $\mathbf{F}(\mathbf{X})$. Thus, the first Piola-Kirchhoff stress is given by,

$$\mathbf{P} = \frac{\partial \psi}{\partial \mathbf{F}}. \tag{4}$$

Given that the strain energy function must also be frame-indifferent, it is redefined as $\psi(\mathbf{C}(\mathbf{X}), \mathbf{X})$ and it is more convenient and common to instead consider the second Piola-Kirchhoff stress,

$$\mathbf{S} = 2\frac{\partial \psi}{\partial \mathbf{C}}, \tag{5}$$

where,

$$\mathbf{C} = \mathbf{F}^T . \mathbf{F}, \tag{6}$$

is the right Cauchy-Green Deformation tensor, which is frame-indifferent by construction. Isotropic strain-energy functions can be expressed as tensor invariants of $\mathbf{C}$ with,

$$I_1 = Tr\,\mathbf{C} \tag{7}$$

$$I_2 = \frac{(Tr\,\mathbf{C})^2 - Tr\,\mathbf{C}^2}{2} \tag{8}$$

$$I_3 = \det \mathbf{C} \tag{9}$$

defining the first, second, and third invariants, respectively. Likewise, the Jacobian determinant,

$$J = \det \mathbf{F} = \sqrt{I_3}, \tag{10}$$

which represents the ratio of the current volume to the reference volume, is a common parameter. Finally, the Cauchy stress follows from the complete push-forward of the second Piola-Kirchhoff stress (Eq. 5),

$$\boldsymbol{\sigma} = \frac{1}{J}\mathbf{F}\,\mathbf{S}\,\mathbf{F}^T. \tag{11}$$

Tissue Scale

A finite element model of confined compression of a full-depth AC specimen was constructed to simulate tissue-scale mechanics. Under confined compression boundary conditions, strain and fluid flux are uniaxial, so the lateral dimensions of the model are arbitrary; therefore, a simple geometry of a thin pillar $25 \times 25 \times 500$ μm in the x, y, and z directions, respectively, was considered. The z direction was aligned perpendicularly to the cartilage surface. All nodes on lateral faces were assigned fixed displacement boundary conditions for their normal components, the lowermost face nodes were fixed in x, y, and z displacement, and the uppermost face nodes were prescribed a vertical displacement of $-25\mu m$ (5% nominal strain) and assigned zero fluid pressure conditions, which corresponds to free-draining. The vertical displacement boundary condition was linearly ramped over a period of 5 seconds corresponding to a constant strain rate of $\frac{1\%}{s}$.

The solid phase constitutive law employed a compressible Holmes-Mow model,[25]

$$\psi = \frac{1}{2}q(e^Q - 1) \tag{12}$$

$$Q = (2\mu - \lambda)(I_1 - 3) + \lambda(I_2 - 3) - (\lambda + 2\mu)\ln J^2 \tag{13}$$

$$q = \frac{\lambda + 2\mu}{2\beta}, \tag{14}$$

to describe the isotropic ground substance. Here the Lamé parameters μ and λ are related to Young's modulus, E, and Poisson's ratio, v, by

$$\lambda = \frac{E}{(1 + v)(1 - 2v)} \tag{15}$$

$$\mu = \frac{E}{2(1 + v)}. \tag{16}$$

The collagen fibre contribution was modelled by a continuous fibre orientation distribution function.[4] In this model, the fibres solely contribute tensile stress determined through integration of the orientation density function in spherical coordinates weighting the contribution of fibres in each direction,

$$\boldsymbol{\sigma}^f = \int_0^{2\pi} \int_0^{\pi} H(I_n - 1)\boldsymbol{\sigma}_n^f(\mathbf{n}^r)\sin\phi d\phi d\theta. \tag{17}$$

Here, the direction $\mathbf{n}^r$ is related to the Cartesian basis $\mathbf{e}_i$ by,

$$\mathbf{n}^r = \cos\theta\sin\phi\,\mathbf{e}_1 + \sin\theta\sin\phi\,\mathbf{e}_2 + \cos\phi\,\mathbf{e}_3, \quad (18)$$

and the invariant

$$I_n = \mathbf{n}^r.\mathbf{C}.\mathbf{n}^r \quad (19)$$

corresponds to the squared fibre stretch in the direction $\mathbf{n}^r$; therefore, the Heaviside function H enforces the tension-only behaviour.[14] As I_n depends on $\mathbf{C}$, Eq. 17 must be integrated at each solution step. The stress contribution in each direction, $\boldsymbol{\sigma}_n^f$, follows from differentiation of the strain energy function,

$$\psi(\mathbf{n}^r, I_n) = \xi(\mathbf{n}^r)(I_n - 1)^{\beta(\mathbf{n}^r)}, \quad (20)$$

where,

$$\xi(\mathbf{n}^r) = \sqrt{\frac{\cos^2\theta\sin^2\phi}{\xi_1} + \frac{\sin^2\theta\sin^2\phi}{\xi_2} + \frac{\cos^2\phi}{\xi_3}} \quad (21)$$

$$\beta(\mathbf{n}^r) = \sqrt{\frac{\cos^2\theta\sin^2\phi}{\beta_1} + \frac{\sin^2\theta\sin^2\phi}{\beta_2} + \frac{\cos^2\phi}{\beta_3}}. \quad (22)$$

The material parameters of this model are thus, ξ_i and β_i along with a provided local basis $\mathbf{e}_i$. In this study, the exponents β_i are all set to 2.0 making fibre stress contribution linear with fibre stretch. ξ_i are varied with depth to reflect the positional change in collagen orientation and thus material anisotropy in cartilage.

The fluid phase behaviour followed Darcy's law (Eq. 3) with deformation-dependent permeability as defined by Holmes and Mow.[25] The permeability varied with volume change,

$$\mathbf{k} = \kappa_0\left(\frac{J - \varphi_0}{1 - \varphi_0}\right)^\alpha e^{\frac{1}{2}M(J^2-1)}. \quad (23)$$

In this study, $\alpha = 2.0$ and $M = 0.0$ for all cartilage positions, reducing the permeability change with J to

$$\mathbf{k} = \kappa_0\left(\frac{J - \varphi_0}{1 - \varphi_0}\right)^2. \quad (24)$$

Reference permeability, κ_0, and solid fraction, φ_0, were varied with depth. Each layer of elements in the z direction were assigned unique material property values based on the position of the element centroids as a fraction of the total AC depth. Univariate splines were used to represent this variation (Fig. 3).

Solid phase parameters were fit to data from Refs. 47 and 59 using sequential quadratic programming[40,57] at each spline point. Depth-wise permeabilities were assumed as those determined in Maroudas et al.[33] Mesh convergence analysis was performed with a discretization with 2500 linear hexahedrons yielding a sufficiently converged solution (Supplementary A).
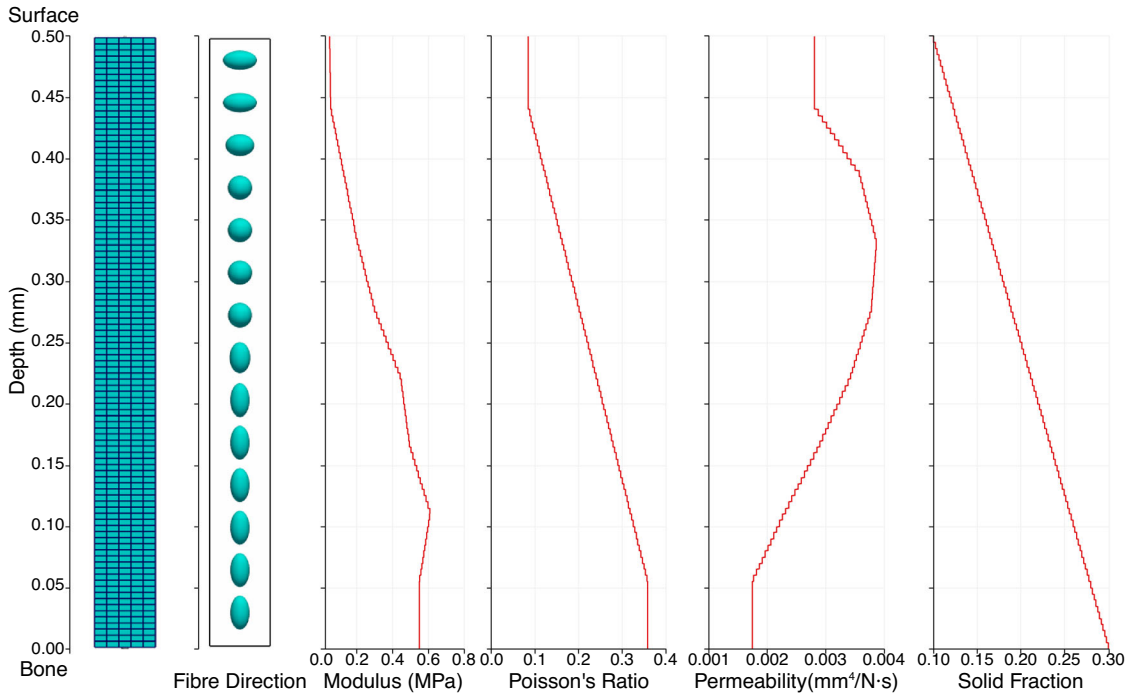
FIGURE 3. A model of confined compression was created to simulate tissue-scale mechanics. Material properties were assigned such that the experimentally observed depth variation was represented. (Left to Right) the discretized model, probability density functions defining the anisotropic contribution of collagen fibres in tension, Young's modulus, Poisson's ratio, hydraulic permeability, and the solid fraction as functions of depth are shown, respectively.

Cellular Scale

A simplified geometric model of a single cell surrounded by PCM and ECM materials was used to investigate the cellular scale mechanics. The cell, PCM, and ECM geometries were modelled as super-ellipsoids, defined by the implicit function,

$$\frac{1}{a}x^\eta + \frac{1}{b}y^\gamma + \frac{1}{c}z^\zeta = 0, \qquad (25)$$

where, a, b, and c are the x-, y-, and z- semi-axes, respectively. The exponents η, γ, and $\zeta \in [2, \infty]$ define the 'squareness' of the super-ellipsoid in the x, y, and z dimensions. At the lower bound of 2 the super-ellipsoid reduces to the ellipsoid, while as the exponents approach infinity the shape approaches a regular parallelepiped. The parameters for the cell, PCM, and ECM are summarized in (Table 2).

To investigate the effect of PCM asymmetry, 3 cases were considered: a 'neutral' case with the cell concentric to the PCM, a 'thin-bottom' case where the cell was vertically shifted $-0.1957\mu m$ so that the PCM thickness on the superior side was 50% thicker than the inferior side, and a 'thin-top' case with the cell vertically shifted $0.1957\mu m$ (Fig. 4). By simply shifting the cell upwards and downwards, the PCM asymmetry

can be modelled while keeping all other geometrical aspects e.g. PCM and ECM volume constant. The ECM, PCM, and cellular regions were discretized with a continuous mesh of linear tetrahedrons that conformed to the regional interfaces. This strategy assumed perfect adhesion between regions and did not require additional specification of contact or tie constraints.

The ECM was assigned the same material model and properties as the tissue scale model through nearest-neighbor interpolation.[25] The material properties of the PCM were likewise interpolated from the ECM, but with scaling factors ($E = 0.1\times$, $v = 1.0\times$, $\beta = 1.0\times$, $k = 1.25\times$).[12,62] Due to the PCM possessing much greater solid phase porosity than the ECM, the M and α parameters of the Holmes-Mow fluid phase model were assumed to be zero, reducing the behaviour to strain-independent permeability. The cellular membrane was modelled with multiphasic shell elements[26] with thicknesses of 10 nm.[3] For the cellular membrane, an isotropic, compressible neo-Hookean,[6]

$$\psi = \frac{\mu}{2}(I_1 - 3) - \mu \ln J + \frac{\lambda}{2}(\ln J)^2, \qquad (26)$$

where Lamé parameters, λ and μ, are related to Young's modulus, $E = 1kPa$, and Poisson's ratio, $v = 0.0$, by Eqs. 15 and 16 constitutive model, described the solid phase. The fluid phase was modelled with a constant, strain-independent permeability ($k = 7 \times 10^{-10} \frac{mm^4}{N \cdot s}$). The low membrane modulus was assigned as a means to simulate the presence of ruffles, which bestow a considerable slack length to the membrane resulting in little solid phase contribution.[18,36] Conversely, the membrane permeability was assumed to be much lower than the surrounding

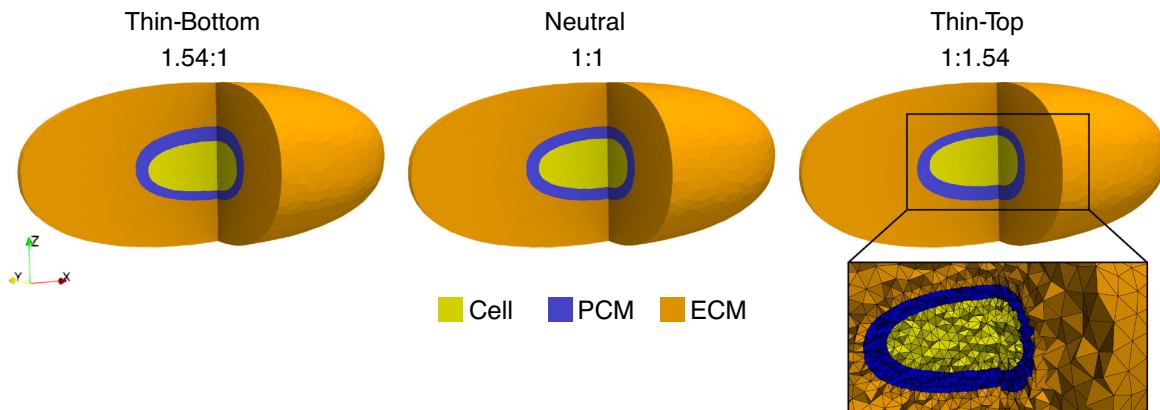**TABLE 2. Super-ellipsoidal parameter values defining geometries of each cellular scale region.**

	a (μm)	b (μm)	c (μm)	η	γ	ζ
Cell	6.0	3.0	2.0	2.3	2.3	2.3
PCM	6.976	3.976	2.9175	2.3	2.3	2.3
ECM	15.03	8.566	6.286	2.3	2.3	2.3

Thin-Bottom	Neutral	Thin-Top
1.54:1	1:1	1:1.54

Cell PCM ECM

FIGURE 4. Three geometric cases were considered at the cellular scale: (left) the cell vertically translated by $0.1957\mu m$ from the PCM centroid resulting in the 'thin-bottom' PCM, (middle) the cell concentric to the PCM for a 'neutral' symmetry case, and (right) the cell vertically translated by $-0.1957\mu m$ from the PCM centroid comprising the 'thin-top' PCM geometry. The ratio between top and bottom PCM thicknesses are shown below each geometry label. A zoomed region is shown on the right to display mesh refinement level and quality.
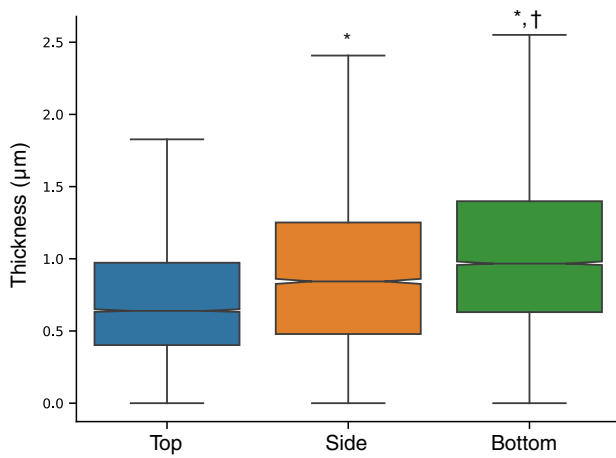
FIGURE 5. Thickness of 'top', 'side' and 'bottom' layers of PCM relative to a cell. The 'top' PCM layer was 35 - 50 % thinner than the 'side' and 'bottom' layers. ∗ indicates significant differences in thickness when compared with the 'top' layer; while † denotes significant differences in thickness when compared with the 'side' layer. Notches indicate the 95% confidence interval in estimated median by bootstrap method with 1000 iterations.

regions as indicated by osmotic swelling experiments.[1] Finally, the cell was modelled as isotropic, compressible neo-Hookean ($E = 1kPa$, $v = 0.0$) with a constant permeability ($k = 1 \times 10^{-3} \frac{mm^4}{N \cdot s}$).

Displacement and fluid pressure boundary conditions were assigned to all surface nodes of the cellular scale model by linearly interpolating the results of the tissue scale model to the cellular scale nodes using the finite element shape functions. This was done at four tissue depths: 10, 20, 30, and 40 μm below the AC surface for each of the three asymmetry cases. Mesh convergence analysis was performed (Supplementary A) with a discretization resolution of 148,066 linear tetrahedrons for the combined ECM, PCM, and cellular volume and 4,846 linear triangles for the membrane determined as sufficient.

RESULTS

Imaging and PCM Segmentation and Morphometrics

A distinct PCM region was identified for all cells analyzed with the novel imaging and segmentation method. When stratified into 'top', 'bottom', and 'side' zones (Fig. 2) significant differences were observed in thickness. The 'bottom' region exhibited the thickest PCM, which differed from both the 'side' ($\approx 14\%$, $p < 0.001$) and 'top' ($\approx 54\%$, $p < 0.001$) zones. The 'side' zone was also significantly thicker ($\approx 35\%$, $p < 0.001$) than the 'top' zone (Fig. 5).

Tissue Scale Simulation

The tissue scale simulation of confined compression to 5% nominal strain over 5 seconds resulted in substantial compaction of the superficial zone relative to deeper tissue (Fig. 6a).

This followed largely from the much softer solid phase properties present in the superficial zone. Since the sole free-draining boundary was the AC surface, fluid fluxes were also the highest in the superficial zone (Fig. 6b).

Cellular Scale Simulations

The cellular scale simulations returned to distinct solutions with regard to membrane deformation. At early times dominated by fluid motion, maximum Green-Lagrange (GL) tensile strains (equivalently the first principal GL strains) on the bottom side of the cell were nearly perpendicular to the cell membrane (Fig. 7a), but oriented tangentially elsewhere. At later times, these eigenvectors were all tangential to the membrane surface (Fig. 7b).

The PCM geometry had a strong influence on the perpendicularly-oriented early stage membrane strains. The 'thin-top' case, which was representative of the quantified PCM thickness, exhibited a marked reduction of approximately 50% in these perpendicularly-oriented maximum GL tensile strains versus the 'neutral' case. Conversely, the opposite of the observed geometry represented by the 'thin-bottom' models, showed an approximate increase of 50% versus neutral. These respective membrane attenuation and

(a)

(b)
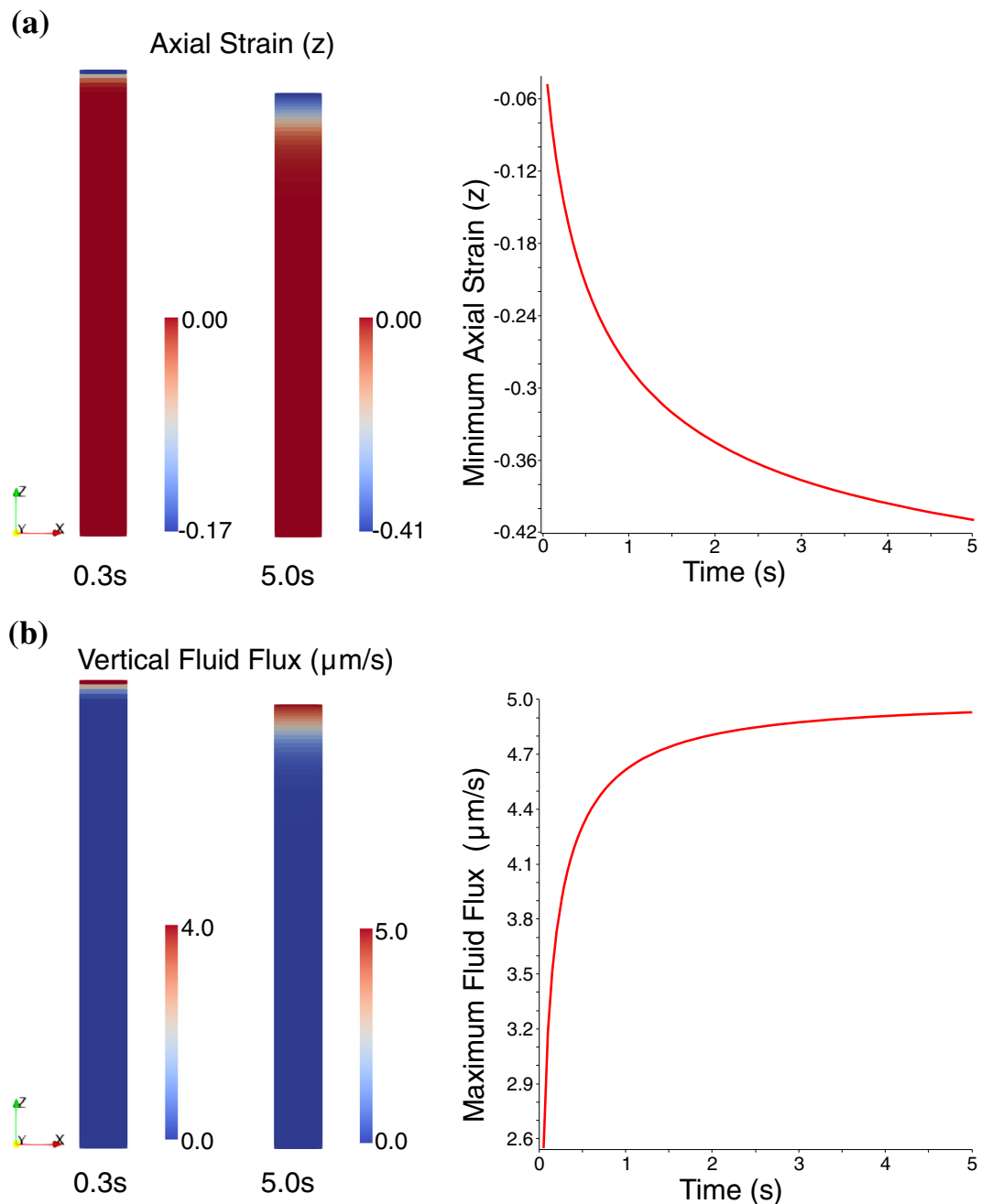
FIGURE 6. (a) The high variability of material properties with depth resulted in large strains concentrated in the superficial zone of the modelled tissue. While the applied nominal strain was only 5% of the total depth, axial compressive Green-Lagrange strains of 0.17 at early deformation stages (0.3 seconds) and 0.41 at the end of the deformation ramp occurred. The minimum Green-Lagrange axial strain (maximum compressive strain) developed non-linearly over the loading interval. At early times, strain magnitudes were low but strain rates were high. Conversely at later times, strains were high but strain rates were lower. (b) Similarly, the fluid fluxes were highest in the superficial zone as this was the only free-draining surface in the simulations.

amplification factors of PCM asymmetry were similar at all simulated depths (top 40 μm).

DISCUSSION

Asymmetric PCM thickness has been previously observed,[44,61,62] but its angular variation around the cells and potential mechanical significance were never
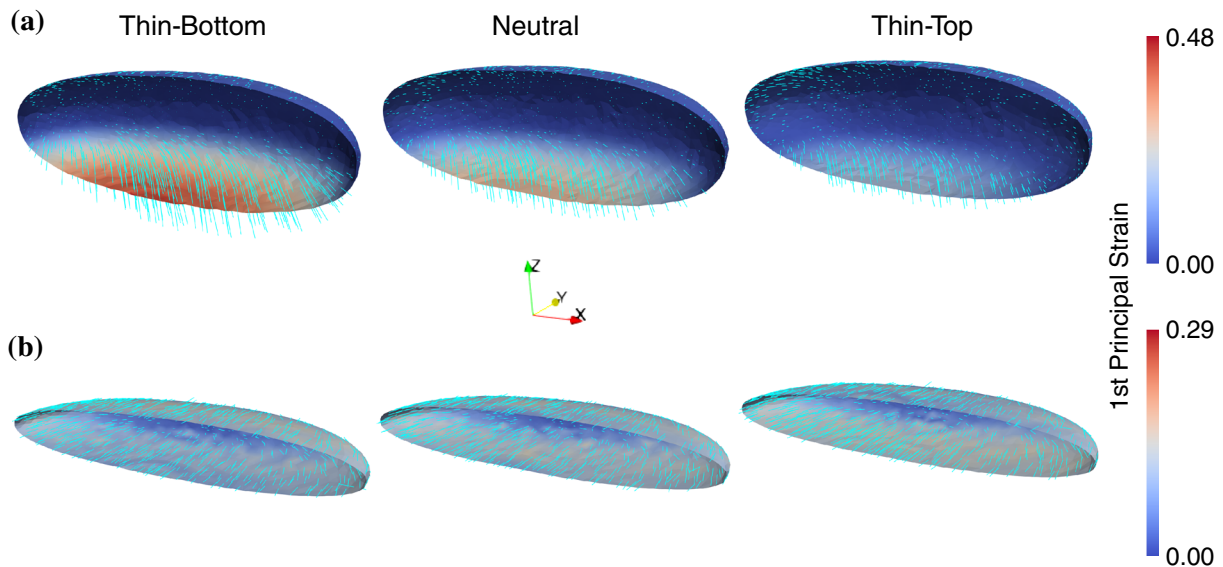
FIGURE 7. The spatial variation of the first principal Green-Lagrange strain of the cellular membrane exhibited two distinct forms over the loading period. The results for simulations at the $10\mu m$ depth are shown here with strain magnitude visualized as color contour plots on the deformed cellular membrane geometry clipped at the mid-plane in the y-direction such that half of the total membrane is seen. Strain magnitude and direction are also also visualized with line glyphs in blue. (a) At early times (0.3*s*) dominated by fluid motion, high tensile strains developed that were directed perpendicular to the membrane surface on the bottom side of the cell. These were reduced by the presence of thicker PCM on the bottom and likewise, increased when the bottom PCM was thinner. (b) At later times when fluid motion was less dominant, tensile strains were oriented tangentially to the cellular membrane.

questioned. Through the use of a novel non-cytotoxic fluorescent staining preparation, multi-photon microscopy, and multi-scale modelling approach this knowledge gap was investigated. Accordingly, the hypothesis that PCM asymmetry was the result of adaptation to mechanical stimuli was addressed. Two criteria for this hypothesis were proposed: 1) that the quantified PCM asymmetry would not be random, but rather directed, and 2) that this directed asymmetry would have non-negligible effects on cellular mechanics. Both of these criteria were satisfied. The PCM asymmetry was strongly directed toward a greater thickness inferior to the cell, approximately 50% thicker than on the superior side. Likewise, this asymmetry majorly attenuated the magnitude of a previously unobserved but potentially dangerous state of cellular deformation that occurred rapidly after the onset of tissue deformation. This cellular deformation was characterized by high magnitude tensile strains oriented nearly perpendicularly to the cellular membrane and localized to the bottom side of the cell (Fig. 7a). In contrast, the typical cellular membrane deformation occurring at most time points features tangentially-oriented tensile strains that tend to uniformity (Fig. 7b).

The use of the recently developed multiphasic shell element[26] to model the cellular membrane was critical for the discovery of these early-stage (occurring several hundreds of milliseconds after load onset), perpendic-

ularly-oriented strains. The extremely low hydraulic permeability of the cellular membrane[1] ($\approx$7 orders of magnitude less than that of the surrounding matrix) was the principal driver of this transient mechanical behaviour. Since fluid motion was impeded across the membrane, it was diverted around the cells such that fluid flux was high above the cell and low below (proportionally fluid pressure was low above and high below) that led to a nearly rigid vertical translation of the cell within the PCM layer (animated video and description in Supplementary B). This cellular translation, in turn, resulted in the development of high tensile strains in the PCM underneath the cell, and likewise perpendicular tensile strains in the cellular membrane (Fig. 8).

Notably, active regulation of membrane permeability, for example, through gating mechanisms of the aquaporin molecular family[8,24] could not be represented in these simulations but, given the large mismatch in permeability between the membrane and the PCM and the rapid dynamics of the system, similar behaviour would be expected even if variable permeability were considered. The magnitude of this flow-induced cellular translation monotonically decreased with tissue depth. Similarly, the translation occurred at earlier times at shallower depths. These two observations were consistent with poroelastic theory, i.e., fluid fluxes were both higher in magnitude and developed earlier at shallower depths (spatially closer to the
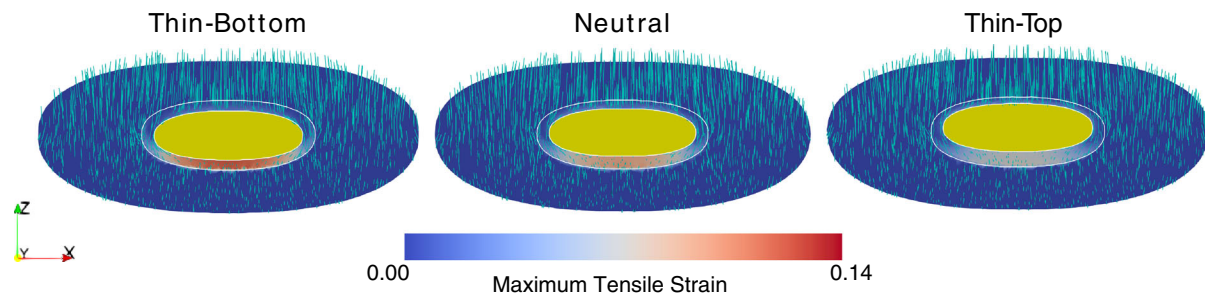
FIGURE 8. The perpendicular tensile membrane strains observed during early deformation (Fig. 7), resulted from a nearly rigid translation of the cell (in yellow) caused by fluid motion. The extremely low permeability of the cellular membrane prevented fluid passage across the cell. The fluid flux was thus directed around the cell, as shown in the overlaid vector plots, resulting in an effective drag. The underlying fringe plots of the maximum tensile Green-Lagrange strain in the ECM and PCM show the development of tensile strain below the cell as a result of this drag. The structural stiffness of the PCM region is determined by its thickness. A thinner PCM material has a higher structural stiffness and *vice versa*. For the 'thin-top' case, cellular translation was slightly attenuated by the stiffer top PCM region, while the resultant tensile strain from a given cellular displacement in the thicker lower PCM was reduced. The opposite effect occurs for the 'thin-bottom' case.
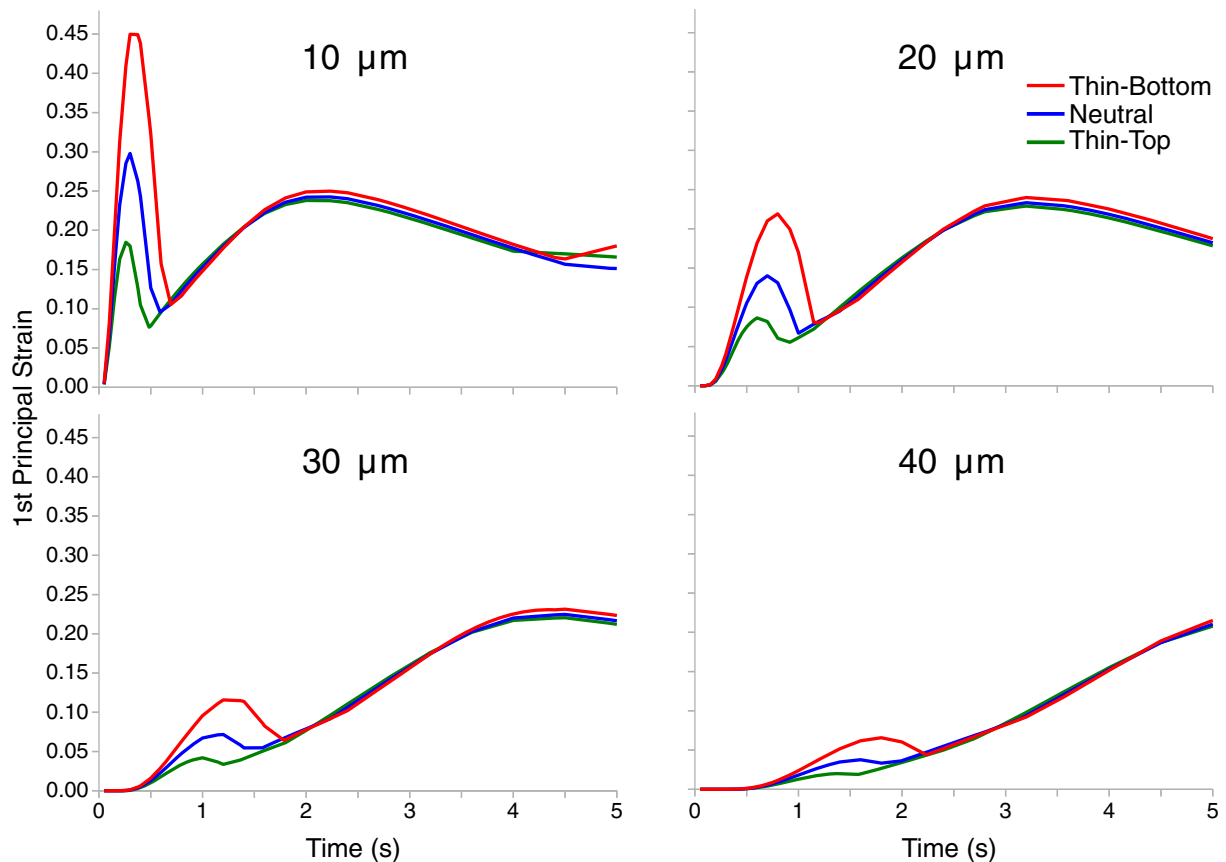

FIGURE 9. An early stage peak in 1st principal Green-Lagrange membrane strain was observed in time series plots for all geometries and at all depths. PCM geometry had a strong influence on this value. The 'thin-top' case attenuated the strain, while the 'thin-bottom' case amplified it. The magnitude of this strain peak monotonically decreased with depth. At the end to the simulated time interval, when fluid motion was less dominant, all PCM geometries exhibited similar strain magnitudes. This was also consistent with depth. All simulated depths 10, 20, 30, and $40\mu m$ correspond to the superficial zone of articular cartilage in rabbit.

draining articular surface). This unique flow-induced membrane strain persisted for a few hundred milliseconds in all simulations, after which the membrane strains became tangentially-oriented with the magnitudes insensitive to the modelled PCM geometry (Fig. 9).

The directed PCM asymmetry strongly affected the magnitude of the perpendicularly-oriented membrane strains during the initial onset of deformation. Models of a 'thin-bottom' PCM (the opposite of the geometry quantified from the experimental observations) resulted in perpendicular membrane strains approximately 3 times higher than the 'thin-top' PCM (the observed geometry) at all depths. Models with equal top and bottom PCM thicknesses ('neutral' PCM), which is the typical representative PCM geometry used in numerical models of chondrocyte mechan-

ics,[20,22,23,37] resulted in perpendicular membrane strains that lie between 1.5 and 2 times that of the 'thin-top' PCM. A concern arose that the imaging procedure employed in this study exhibited a bias towards a thinner PCM thickness measurement than past studies that reported PCM thickness of approximately $3\mu m$. This concern was addressed by generating models of the three geometric cases with the PCM thickness proportionally increased to an average value of $3\mu m$. The mechanical effect of PCM asymmetry was further enhanced in simulations with these scaled geometries; such that the perpendicular membrane strains found in the 'thin-bottom' PCM increased to 5 times those of the 'thin-top' PCM (Fig. 10).

Interestingly, the overall PCM thickness has been observed to increase with osteoarthritis progression.[45,50] The increased effect of PCM asymmetry in
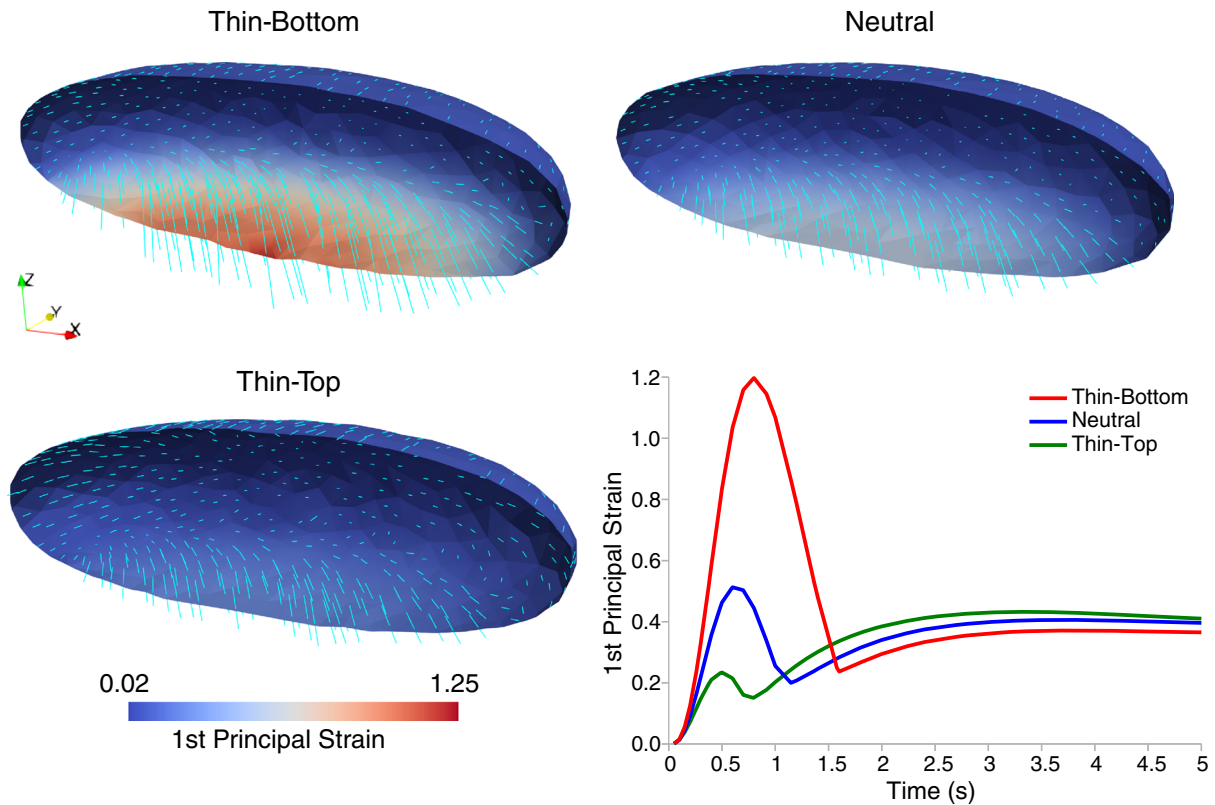
FIGURE 10. **Simulations with the PCM thickness scaled to $3\mu m$, while maintaining the same asymmetry ratios, exhibited similar behaviour in the 1st principal Green-Lagrange strain of the cell membrane. The 1st principal strains are shown at the time points when they were maximal for each symmetry case represented with both line glyphs in blue and contour plots of strain magnitude on the the cellular membrane geometry clipped at its midsection. These cellular scale models were located at $13\mu m$ from the tissue top surface; the shallowest depth simulated for the scaled case. The attenuation effects on tensile strains perpendicular to the membrane of a thicker PCM beneath the cell were even more pronounced for this scaled geometry. The 'thin-bottom' case exhibited nearly $4\times$ higher strains than the 'thin-top' case. The lower-right panel shows the highest value for the 1st principal Green-Lagrange strain at all time points of the simulation. There was a temporal shift in the early time peaks between asymmetry cases with the maximum occurring for the 'thin-bottom' case at 0.8, the 'neutral' case at 0.6, and the 'thin-top' case at 0.5 seconds, respectively.**

the scaled models may thus have important implications for cellular mechanics in diseased tissue; particularly, if the asymmetry ratios remain similar. Regardless, both the results of the simulations with original and scaled geometries indicate that synthesis of thicker PCM beneath the cell may be a mechanical adaptation to reduce the perpendicular membrane strains. The question thus follows, how may the development of such a strain state be undesirable or dangerous to chondrocyte integrity?

It is known that the chondrocyte membrane can withstand high tangentially-oriented membrane strains through unfolding of its ruffled structures.[18,36] However, it may not have such exceptional resilience when exposed to the localized perpendicularly-oriented strains revealed in these simulations. Indeed, such strains may have profound effects on cellular attachment to the surrounding environment through, for instance, focal adhesions (FAs). Formation of FAs is mediated by transmembrane proteins called integrins that connect the cellular cytoskeleton and the PCM. FAs provide one avenue for cells to effectively sense and respond to their local mechanical environment and are critical to normal homeostasis.[46,58] However, FAs are among the weaker components in the cell attachment machinery as shown by experiments with cells exposed to fluid-induced shear stress.[16] Some parallels may also be drawn from measurements using atomic force microscopy to pull the membrane perpendicularly with nanotube membrane tethers, which showed a strong rate dependence.[35] In that study, membrane nanotubes remained attached for much greater pulling lengths when the pulling rate was low. This behaviour was hypothesized to result from viscous effects preventing the membrane from unfolding quickly enough during the high rate pulls causing high forces at the tethers leading to earlier detachment. Analogously, high strain rates during the development of the perpendicular membrane strains in the current study may also prevent access to the membrane unfolding and high forces at the FAs, possibly leading to detachment. Other cell-matrix interactions, such as calcium activated adhesions (cadherins) mediated by the CD44 antigen, may also be interrupted by the perpendicular membrane strain. Loss of these cell-matrix interactions often negatively impact the metabolism of the cartilage.[29] The presented simulation results suggest that an increased PCM thickness underneath the cell reduces both the perpendicular membrane strain magnitude and its rate, analogous to the pulling length and pulling rate of the nano-tether experiments, respectively. In addition to the interruption to cell-matrix interactions, the localized high magnitude tension may lead to membrane rupture; however, this statement would need further investigation especially for the case of cells *in situ*. The continuum mechanics modelling employed here, while providing hints to the underlying phenomena, lacks the scope and resolution to explore the localized mechanics of focal adhesion. In the future, molecular dynamics experimentation and modelling aimed at protein-lipid bilayer physics may be warranted to further illuminate the mechanics at the nano-scale of FAs.[27]

Additional evidence for asymmetrical PCM adaptation in cartilage may have been overlooked in past studies. For example, the transmission electron micrograph in Fig. 2 of Moo et al.[36] (Supplementary D), shows a clear bias towards membrane ruffle formation on the inferior side of the cell. While a single micrograph is anecdotal, an extended analysis for ruffle asymmetry in the full dataset of this work would be of great interest. Intuitively, such membrane asymmetry may be a co-adaptation along with PCM thickness asymmetry to the perpendicular membrane strains herein discussed.

The utilized sample preparation and imaging protocol offers several advantages over past methods. Previous investigations of PCM geometry were limited to immunochemical staining approaches that required tissue fixation, which invariably leads to total cell death and alteration of the tissue mechanical properties.[44,61,62] Here, the dual-labeling technique using low concentration 5-DTAF aminoflourescein and calcein red/orange AM for the ECM and cells, respectively, allowed for probing of live tissue with minimal changes to bulk mechanical properties.[53] Although DTAF binds non-specifically to many types of collagen,[30] the difference in local concentration of total collagen in the ECM vs the PCM allowed for the detection of the PCM layer as a region with low fluorescence intensity (Fig. 2, see also Supplementary C for more details). Nevertheless, the average measured thickness of the PCM (1–2 μm) were consistently less than those observed with immunostaining (2–4 μm). This is due to the diffuse, radial variation of collagen content away from cells, and the hard boundary determined for the PCM region through application of a consistent segmentation protocol (see Methods). As the main objective of this study was to morphometrically quantify PCM asymmetry, this systematic underestimation of PCM thickness, was of less concern because the ratios in thickness were expected to remain similar. Alternatively, this imaging protocol could be used to quantify the variation in collagen content transitioning radially from the cell to the ECM through consideration of the level-set variation of image intensity.

There are limitations to this study that need to be considered for proper interpretation of the presented results. The quantification of PCM asymmetry was limited to superficial zone cells and a single species.

The method, however, can be easily applied to cells of other zones and in different species. An investigation into the PCM asymmetry for cells in other zones is a critical next step. Under the assumption that the cellular motion induced by high fluid drag near the AC surface generates perpendicular membrane strains and leads to an asymmetry adaptation, it should follow that cells farther from the surface will exhibit less asymmetry bias. Should such a trend with AC depth be observed, it would further support the proposed adaptation hypothesis. The confined compression boundary conditions assigned for the tissue scale simulations are not representative of physiological loading of cartilage. The confined compression condition will result in higher fluid fluxes at the top surface and higher fluid pressurization of deeper zones than the opposite extreme of unconfined compression. The physiological loading of cartilage lies somewhere between these two extremes. Similarly, the magnitude and rate of the compression in the tissue scale simulations (5% at $\frac{1\%}{s}$) was lower than physiological. Investigating the hypotheses reported here for more physiological tissue scale mechanics is certainly warranted. Likewise, at the cellular scale, idealized geometry representative of PCM asymmetry on average was considered. This allowed for systematic investigation of the asymmetry effects, but may not reflect the behaviour of realistic cellular and PCM geometry.

The assignment of PCM material properties as scaled values of the corresponding local ECM parameters was a modelling design choice. It has been well established through measurement with atomic force microscopy that the PCM is mechanically softer than the local ECM,[12,62] and that this relative difference in elastic modulus has strain modulation effects on the cell.[9] However, the proportionality of the PCM properties to the surrounding ECM may have strong influence on such mechanical modulation. While the intent of this study was to assess the geometric consequences of the PCM, additional investigation of assumed scaling factors of the PCM to the ECM would also be of value.

Characterization in pathological tissue and quantification of local mechanics using non-destructive photobleaching of a grid to aid deformable image registration at different stages of progression would also be of interest. Likewise, once better understood, the addition of a PCM asymmetry metric in histological analysis and grading may be of merit. The deformation behaviour of the PCM may also be evaluated using a optico-mechanical testing system and deformable image registration.[38] In the realm of tissue engineering, encouraging appropriate PCM asymmetry may be a currently unexplored but useful strategy for producing a yet-to-be-realized functional AC substitute.

CONCLUSION

While additional investigation of PCM asymmetry beyond this initial work is certainly warranted, the current findings hold substantial weight. The asymmetry in PCM thickness between top and bottom regions was of considerable magnitude (54%), established from a large sample (355 chondrons), and of high statistical confidence ($p < 0.001$). The membrane mechanics calculated with the modelling and simulation protocol were likewise persuasive, with the strain magnitudes approximately halved in the models with observation-based asymmetrical geometry versus those with a symmetrical PCM. This strong geometric effect along with the discussed biophysics-based dangers to lipid membrane integrity and FA attachments further reinforce the potential for PCM asymmetry having a cellular protective role. In light of these experimental and simulated observations, it is concluded that PCM asymmetry may very likely play a critical role in chondrocyte and tissue health and merit further investigation and scrutiny.

SUPPLEMENTARY INFORMATION

The online version contains supplementary material available at https://doi.org/10.1007/s10439-021-02900-1.

AUTHOR CONTRIBUTIONS

S.C.S and E.K.M. conceived the microscopy protocol. E.K.M. conducted the sample harvest, preparation, and microscopy. S.C.S generated and performed image segmentation and analysis. S.C.S. designed and conducted the modelling and simulation. S.C.S and E.K.M analyzed the results. S.F. and W.H. provided scientific and mathematical guidance. All authors reviewed the manuscript.

CONFLICT OF INTEREST

The authors do not have any conflicts of interest with regard to this work to disclose.

ACKNOWLEDGMENTS

REFERENCES

[1] Albro, M. B., L. E. Petersen, R. Li, C. T. Hung, and G. A. Ateshian. Influence of the partitioning of osmolytes by the cytoplasm on the passive response of cells to osmotic loading. *Biophys. J.* 97:2886–2893, 2009.

[2] Alexopoulos, L. G., I. Youn, P. Bonaldo, and F. Guilak. Developmental and Osteoarthritic Changes in Col6a1 Knockout Mice: The Biomechanics of Collagen VI in the Cartilage Pericellular Matrix. *Arthritis Rheum.* 60:771–779, 2009.

[3] Ateshian, G. A., K. D. Costa, and C. T. Hung. A theoretical analysis of water transport through chondrocytes. *Biomech. Model. Mechanobiol.* 6:91–101, 2007.

[4] Ateshian, G. A., V. Rajan, N. O. Chahine, C. E. Canal, and C. T. Hung. Modeling the matrix of articular cartilage using a continuous fiber angular distribution predicts many observed phenomena. *J. Biomech. Eng.* 131:061003, 2009.

[5] Aviezer, D., D. Hecht, M. Safran, M. Eisinger, G. David, and A. Yayon. Perlecan, basal lamina proteoglycan, promotes basic fibroblast growth factor-receptor binding, mitogenesis, and angiogenesis. *Cell* 79:1005–1013, 1994.

[6] Bonet, J. and R. Wood. Nonlinear Continuum Mechanics for Finite Element Analysis. Cambridge: Cambridge University Press 1997.

[7] Chery, D. R., B. Han, Q. Li, Y. Zhou, S.-J. Heo, B. Kwok, P. Chandrasekaran, C. Wang, L. Qin, X. L. Lu, D. Kong, M. Enomoto-Iwamoto, R. L. Mauck, and L. Han. Early changes in cartilage pericellular matrix micromechanobiology portend the onset of post-traumatic osteoarthritis. *Acta Biomaterialia* 111:267–278, 2020.

[8] Cho, S.-J., A. K. M. A. Sattar, E.-H. Jeong, M. Satchi, J. A. Cho, S. Dash, M. S. Mayes, M. H. Stromer, and B. P. Jena. Aquaporin 1 regulates GTP-induced rapid gating of water in secretory vesicles. *Proc. Natl. Acad. Sci.* 99:4720–4724, 2002.

[9] Choi, J. B., I. Youn, L. Cao, H. A. Leddy, C. L. Gilchrist, L. A. Setton, and F. Guilak. Zonal changes in the three-dimensional morphology of the chondron under compression: the relationship among cellular, pericellular, and extracellular deformation in articular cartilage. *J. Biomech.* 40:2596–2603, 2007.

[10] Chuang, C. Y., M. S. Lord, J. Melrose, M. D. Rees, S. M. Knox, C. Freeman, R. V. Iozzo, and J. M. Whitelock. Heparan Sulfate-Dependent Signaling of Fibroblast Growth Factor 18 by Chondrocyte-Derived Perlecan. *Biochemistry* 49:5524–5532, 2010.

[11] Cohen, N. P., R. J. Foster, and V. C. Mow. Composition and dynamics of articular cartilage: structure, function, and maintaining healthy state. *J. Orthopaed. Sports Phys.Therapy* 28:203–215, 1998.

[12] Darling, E. M., R. E. Wilusz, M. P. Bolognesi, S. Zauscher, and F. Guilak. Spatial mapping of the biomechanical properties of the pericellular matrix of articular cartilage measured in situ via atomic force microscopy. *Biophys. J.* 98:2848–2856, 2010.

[13] Dimicco, M. A., J. D. Kisiday, H. Gong, and A. J. Grodzinsky. Structure of pericellular matrix around agarose-embedded chondrocytes. *Osteoarthritis Cartil.* 15:1207–1216, 2007.

[14] Federico, S., and W. Herzog. Towards an analytical model of soft tissues. *J. Biomech.* 41:3309–3313, 2008.

[15] Felson, D. T. Identifying different osteoarthritis phenotypes through epidemiology. *Osteoarthritis Cartil.* 18:601–604, 2010.

[16] Fuhrmann, A. and A. Engler. The cytoskeleton regulates cell attachment strength. *Biophys. J.* 109:57–65, 2015.

[17] Grässel, S. and D. Muschter. Recent advances in the treatment of osteoarthritis. *F1000Research* 9, 2020.

[18] Guilak, F., G. R. Erickson, and H. P. Ting-Beall. The effects of osmotic stress on the viscoelastic and physical properties of articular chondrocytes. *Biophys. J.* 82:720–727, 2002.

[19] Guilak, F., H. A. Leddy, and W. Liedtke. Transient receptor potential vanilloid 4: the sixth sense of the musculoskeletal system? *Ann. N. Y. Acad. Sci.* 1192:404–409, 2010.

[20] Guilak, F. and V. C. Mow. The mechanical environment of the chondrocyte: a biphasic finite element model of cell-matrix interactions in articular cartilage. *J. Biomech.* 33:1663–1673, 2000.

[21] Guilak, F., R. J. Nims, A. Dicks, C.-L. Wu, and I. Meulenbelt. Osteoarthritis as a disease of the cartilage pericellular matrix. *Matrix Biol.* 71–72:40–50, 2018.

[22] Guo, H. and P. A. Torzilli. Shape of chondrocytes within articular cartilage affects the solid but not the fluid microenvironment under unconfined compression. *Acta Biomater.* 29:170–179, 2016.

[23] Han, S.-K., S. Federico, and W. Herzog. A depth-dependent model of the pericellular microenvironment of chondrocytes in articular cartilage. *Comput. Methods Biomech. Biomed. Eng.* 14:657–664, 2011.

[24] Hedfalk, K., S. Törnroth-Horsefield, M. Nyblom, U. Johanson, P. Kjellbom, and R. Neutze. Aquaporin gating. *Curr. Opin. Struct.Biol.* 16:447–456, 2006.

[25] Holmes, M. H. and V. C. Mow. The nonlinear characteristics of soft gels and hydrated connective tissues in ultrafiltration. *J. Biomech.* 23:1145–1156, 1990.

[26] Hou, J. C., S. A. Maas, J. A. Weiss, and G. A. Ateshian. Finite element formulation of multiphasic shell elements for cell mechanics analyses in FEBio. *J. Biomech. Eng.* 2018.

[27] King, G. M. and I. Kosztin. Towards a quantitative understanding of protein-lipid bilayer interactions at the single molecule level: opportunities and challenges. *J. Membr. Biol.* 254:17–28, 2021.

[28] Kirn-Safran, C., M. C. Farach-Carson, and D. D. Carson. Multifunctionality of extracellular and cell surface heparan sulfate proteoglycans. *Cell. Mol. Life Sci.* 66:3421–3434, 2009.

[29] Knudson, W. and R. F. Loeser. CD44 and integrin matrix receptors participate in cartilage homeostasis. *Cell. Mol. Life Sci.* 59:36–44, 2002.

[30] Krahn, K. N., C. V. C. Bouten, S. van Tuijl, M. A. M. J. van Zandvoort, and M. Merkx. Fluorescently labeled collagen binding proteins allow specific visualization of collagen in tissues and live cell culture. *Analyt. Biochem.* 350:177–185, 2006.

[31]Lowekamp, B. C., D. T. Chen, L. Ibáñez, and D. Blezek. The design of simpleITK. *Front. Neuroinf.* 7, 2013.

[32]Maas, S. A., B. J. Ellis, G. A. Ateshian, and J. A. Weiss. FEBio: finite elements for biomechanics. *J. Biomech. Eng.* 134:011005, 2012.

[33]Maroudas, A. and P. Bullough. Permeability of articular cartilage. *Nature* 219:1260–1261, 1968.

[34]Moo, E. K., Z. Abusara, N. A. Abu Osman, B. Pingguan-Murphy, and W. Herzog. Dual photon excitation microscopy and image threshold segmentation in live cell imaging during compression testing. *J. Biomech.* 46:2024–2031, 2013.

[35]Moo, E. K., M. Amrein, M. Epstein, M. Duvall, N. A. Abu Osman, B. Pingguan-Murphy, and W. Herzog. The properties of chondrocyte membrane reservoirs and their role in impact-induced cell death. *Biophys.J.* 105:1590–1600, 2013.

[36]Moo, E. K. and W. Herzog. Unfolding of membrane ruffles of in situ chondrocytes under compressive loads. *J. Orthop. Res.* 35:304–310, 2017.

[37]Moo, E. K., W. Herzog, S. K. Han, N. A. Abu Osman, B. Pingguan-Murphy, and S. Federico. Mechanical behaviour of in-situ chondrocytes subjected to different loading rates: a finite element study. *Biomech. Model. Mechanobiol.* 11:983–993, 2012.

[38]Moo, E. K., S. C. Sibole, S. K. Han, and W. Herzog. Three-dimensional micro-scale strain mapping in living biological soft tissues. *Acta Biomaterialia* 70:260–269, 2018.

[39]Mow, V. C., S. C. Kuei, W. M. Lai, and C. G. Armstrong. Biphasic Creep and Stress Relaxation of Articular Cartilage in Compression: Theory and Experiments. *J. Biomech. Eng.* 102:73–84, 1980.

[40]Nocedal, J. and S. J. Wright. Numerical Optimization. Springer Series in Operations Research. New York: Springer 2006, 2nd ed edition.

[41]O'Conor, C. J., N. Case, and F. Guilak. Mechanical regulation of chondrogenesis. *Stem Cell Res.Therapy* 4:61, 2013.

[42]Ojanen, S. P., M. A. J. Finnilä, A. E. Reunamo, A. P. Ronkainen, S. Mikkonen, W. Herzog, S. Saarakkala, and R. K. Korhonen. Site-specific glycosaminoglycan content is better maintained in the pericellular matrix than the extracellular matrix in early post-traumatic osteoarthritis. *PLoS ONE* 13:e0196203, 2018.

[43]Otsu, N. A threshold selection method from gray-level histograms. *IEEE Trans. Syst. Man Cybern.* 9:62–66, 1979.

[44]Poole, C., S. Ayad, and J. Schofield. Chondrons from articular cartilage: I. Immunolocalization of type VI collagen in the pericellular capsule of isolated canine tibial chondrons. *J. Cell Sci.* 90 (Pt 4):635–643, 1988.

[45]Poole, C. A., A. Matsuoka, and J. R. Schofield. Chondrons from articular cartilage. III. Morphologic changes in the cellular microenvironment of chondrons isolated from osteoarthritic cartilage. *Arthritis Rheum.* 34:22–35, 1991.

[46]Qu, F., F. Guilak, and R. L. Mauck. Cell migration: implications for repair and regeneration in joint disease. *Nat. Rev.* 15:167–179, 2019.

[47]Schinagl, R. M., D. Gurskis, A. C. Chen, and R. L. Sah. Depth-dependent confined compression modulus of full-thickness bovine articular cartilage. *J. Orthop. Res.* 15:499–506, 1997.

[48]Schroeder, W., K. Martin, and B. Lorensen. The Visualization Toolkit, Kitware, Inc. 2006, 4 edition.

[49]Smith, S. M. L., L. A. West, P. Govindraj, X. Zhang, D. M. Ornitz, and J. R. Hassell. Heparan and chondroitin sulfate on growth plate perlecan mediate binding and delivery of FGF-2 to FGF receptors. *Matrix Biol.* 26:175–184, 2007.

[50]Söder, S., L. Hambach, R. Lissner, T. Kirchner, and T. Aigner. Ultrastructural localization of type VI collagen in normal adult and osteoarthritic human articular cartilage. *Osteoarthritis Cartil.* 10:464–470, 2002.

[51]Stark, J. A. Adaptive image contrast enhancement using generalizations of histogram equalization. *IEEE Trans. Image Process.* 9:889–896, 2000.

[52]SundarRaj, N., D. Fite, S. Ledbetter, S. Chakravarti, and J. Hassell. Perlecan is a component of cartilage matrix and promotes chondrocyte attachment. *J. Cell Sci.* 108:2663–2672, 1995.

[53]Szczesny, S. E., R. S. Edelstein, and D. M. Elliott. DTAF dye concentrations commonly used to measure microscale deformations in biological tissues alter tissue mechanics. *PLoS ONE* 9:e99588, 2014.

[54]Tillet, E., H. Wiedemann, R. Golbik, T.-C. Pan, R.-Z. Zhang, K. Mann, M.-L. Chu, and R. Timpl. Recombinant expression and structural and binding properties of $\alpha 1$(VI) and $\alpha 2$(VI) chains of human collagen type VI. *Eur. J. Biochem.* 221:177–187, 1994.

[55]Tomasi, C. and R. Manduchi. Bilateral filtering for gray and color images. In: Proceedings of the IEEE International Conference on Computer Vision, pp. 839–846, Bombay, India1998.

[56]Torzilli, P. A. and V. C. Mow. On the fundamental fluid transport mechanisms through normal and pathological articular cartilage during function-I. The formulation. Journal of Biomechanics 9:541–552, 1976.

[57]Virtanen, P., R. Gommers, T. E. Oliphant, M. Haberland, T. Reddy, D. Cournapeau, E. Burovski, P. Peterson, W. Weckesser, J. Bright, S. J. van der Walt, M. Brett, J. Wilson, K. J. Millman, N. Mayorov, A. R. J. Nelson, E. Jones, R. Kern, E. Larson, C. J. Carey, Ä. Polat, Y. Feng, E. W. Moore, J. VanderPlas, D. Laxalde, J. Perktold, R. Cimrman, I. Henriksen, E. A. Quintero, C. R. Harris, A. M. Archibald, A. H. Ribeiro, F. Pedregosa, P. van Mulbregt, and SciPy 1.0 Contributors. SciPy 1.0: fundamental algorithms for scientific computing in Python. *Nat. Methods* 17:261–272, 2020.

[58]Vogel, V. and M. Sheetz. Local force and geometry sensing regulate cell functions. *Nat. Rev.* 7:265–275, 2006.

[59]Wang, C. C. B., N. O. Chahine, C. T. Hung, and G. A. Ateshian. Optical determination of anisotropic material properties of bovine articular cartilage in compression. *J. Biomech.* 36:339–353, 2003.

[60]Whitaker, R. and X. Xue. Variable-conductance, level-set curvature for image denoising. In: IEEE International Conference on Image Processing, volume 3, pp. 142–145, Thessaloniki, Greece 2001.

[61]Wilusz, R. E., L. E. Defrate, and F. Guilak. A biomechanical role for perlecan in the pericellular matrix of articular cartilage. *Matrix Biol.* 31:320–327, 2012.

[62]Wilusz, R. E., L. E. DeFrate, and F. Guilak. Immunofluorescence-guided atomic force microscopy to measure the micromechanical properties of the pericellular matrix of porcine articular cartilage. *J. R. Soc. Interface* 9:2997–3007, 2012.

[63]Wilusz, R. E., J. Sanchez-Adams, and F. Guilak. The structure and function of the pericellular matrix of articular cartilage. *Matrix Biol.* 39:25–32, 2014.

[64]Zelenski, N. A., H. A. Leddy, J. Sanchez-Adams, J. Zhang, P. Bonaldo, W. Liedtke, and F. Guilak. Collagen VI regulates pericellular matrix properties, chondrocyte swelling,

and mechanotransduction in articular cartilage. *Arthritis & Rheumatol. (Hoboken, N.J.)* 67:1286–1294, 2015.

[65]Zipfel, W. R., R. M. Williams, and W. W. Webb. Nonlinear magic: multiphoton microscopy in the biosciences. *Nat. Biotechnol.* 21:1369–1377, 2003.